

Developing Vibrational Infrared Near Field Spectroscopy to Characterize Polymer Structures on Surfaces: Identification and Reduction of Topographic Coupling Artifacts

Boris B. Akhremitchev and Gilbert C. Walker*

Department of Chemistry, University of Pittsburgh, Pittsburgh, PA 15260, USA

(Received September 19, 2001)

We report efforts to develop infrared near field microscopy for the characterization of polymer surfaces. The new near field microscope is adapted from an atomic force microscope with custom optics to create a high spatial resolution imaging platform. In addition, we report developments of analytical and finite difference approaches relating the rough sample/light interaction, the resultant near field optical signal, and the chemical structure of the sample. Simulations of the role of a topographic coupling artifact of the observed near field signal, and a method to overcome that artifact are presented.

There are well-established methods for studying phase separation in bulk polymers, such as light scattering, small angle neutron scattering, and pulsed NMR techniques.[1] Unfortunately, these methods are not suitable for studying surface phenomena. On the other hand, there are classical methods of surface analysis.[2] These methods often require ultra high vacuum and can be expensive. With advent of scanning probe microscopes investigations of surfaces on mesoscopic scales in air or even in liquid have become possible.[3,4,5,6,7,8,9,10]

The combination of atomic force microscopy (AFM) and near field scanning optical micrcoscopy (NSOM) is a promising development in scanning probe microscopy. NSOM provides optical images with resolution much higher than conventional micoscopy, even scanning laser confocal microscopy. Using infrared (IR) radiation can enable investigation of specific vibrational transitions, providing high local contrast and imaging of different chemical groups on the polymer surface. The intensity dependence of the detected NSOM radiation on polarization of the incident light can provide information on local bond structuve orientations. Sequential date acquisition will provide the time dependence of the local properties listed above.

Developments in near field infrared spectroscopy can provide novel information about chemical organization of polymeric surfaces on 10^{-8}–10^{-5} m scale. This information is important for both fundamental and applied sciences; it will reveal the thermodynamics and kinetics of phase separation, elucidate the mechanisms of intermolecular interaction, and help to develop models of the surface properties of polymers, thus facilitating new materials design.

We are developing the combination AFM and NSOM to address some basic questions about polymer film surfaces: On what length scale is the chemical composition of the surface heterogeneous? Can typical samples, which are usually rough, be imaged by near field microscopy for chemical content?

A variety of new techniques have been invented since the introduction of scanning probe microscopes. One technique is scanning near-field optical microscopy. This method allows one to obtain optical images with lateral resolution beyond the well-known far-field diffraction limit of (Rayleigh criteria):

$$r_{\min} > 1.22\lambda/(2n\sin(\theta)) \quad (1)$$

Here $r_{\min}$ is the limit of resolution, λ is wavelength of the light, n is the index of refraction of the medium, and θ is the acceptance angle of the objective. There are three obvious ways to improve resolution ($1/r$) in the far field limit: a) decrease the wavelength, which leads to the well-established technique of electron microscopy; b) increase the indices of refraction of the media; c) increase the numerical aperture of the microscope objective. Even for immersion objectives with high numerical apertures, $\lambda/2$ remains the limiting optical resolution. And electron microscopy, given its high resolution, does not easily provide chemical information about an object and requires vacuum conditions.

We now consider briefly what is actually detected by the optical microscope. A conventional microscopes optical system creates an optical image, a far field image. Non-propagating fields near the surface of an object under study will *not* be imaged by such a microscope. Even the emitting point dipole looks like a sphere of approximately $\lambda/2$ in diameter when viewed by the optical microscope. Inside such a "sphere" there is a non-propagating electromagnetic field. A non-propagating field exists in the vicinity of any light scattering or emitting object with spatial variations of optical properties on a length scale less than the wavelength of the light. Such a near-field zone is confined to the surface; for an optical wavelength it is usually a few hundred nanometers.

One way to obtain optical information on a subwavelength scale is to perturb components of the near-field with a small test object. Such object can convert a non-propagating field into a propagating one (and vice versa, a propagting field into

an evanescent one) which can be detected by a remote sensor in the far field. This idea is based on the fact that a small object can convert incident radiation (propagating or non-propagating) into both components[11] and is the basis for most scanning optical microscopes. It was first proposed by Synge in 1928.[12] His idea is to use a flat sample with divergence from the true plane that is less than 10 nm over the sampled area and an opaque flat screen with a minute aperture (less than 10 nm diameter). The screen should be kept a few nanometers away from the sample and illuminated with a very bright light source. A small amount of light transmitted through the aperture (and then the sample) may be detected. Scanning the sample induces changes in transmitted light, thus making an optical image with resolution corresponding to the size of the hole. Synge pointed out several experimental difficulties, such as low light source brightness and the positioning accuracy necessary to perform measurements. This kind of microscopy became possible with the invention of the laser in the middle 60's and scanning microscopes in the early 80's, Another problem that Synge considered was the manufacture of the minute aperture. One contemporary solution is to use a small aperture at the end of an optical fiber. A theoretical calculation regarding the intensity of the light transmitted through small aperture was accomplished by Bethe.[13]

The implementation of this technique was first reported for 3 cm microwave radiation by Ash and Nicholes in 1972.[14] They achieved $\lambda/200$ resolution. The first publication showing resolution of near-field *optical*-scanning microscope appeared in 1984[3] by Pohl and co-workers from IBM Zurich Research Laboratory. Similar, early experiments were accomplished at Cornell University.[5]

Following Synge, a contemporary near-field microscope consists of a probe scanning near the sample surface, a light source, a distance controller and a far-field detector. There are several variations on this basic microscope. The designs differ mostly by how the probe is included. The probe can be used as a light emitter, a light collector or both. An alternative approach is to use a probe to perturb the light scattered by the sample object. Here only two configurations are mentioned: the most common one and the one of particular interest to us.

In the common configuration the probe is a tapered optical fiber with a tiny aperture at its very sharp apex. This fiber tip is used as an illumination source. To avoid problems with stray light the fiber is coated with aluminum. Because of the finite conductivity of aluminum at optical frequencies, the coating needs to be rather thick—several skin-layers thick (about 100 nm). Light from a light source (gas or diode laser) is coupled to the fiber producing a tiny light source.

Sample and probe positioning is performed using XYZ piezo-electric ceramic stages. There are several techniques available to control the tip-sample separation, the most common one is the so-called "shear force" feedback. Laser light is focused near the probe's apex and the shadow is positioned onto a two element photodetector. Vibrating the tip parallel to the sample surface produces an AC current in the photodiode circuit. When the tip approaches surface, shear forces damp tip vibration, thus providing indication of the surface proximity. Feedback circuitry maintains a constant amplitude of tip oscillation via tip or sample displacement. This provides constant height operation of the apparatus. Light scattered by the sample is collected by the microscope objective and transferred to photomultiplier. Scanning the smaple in the X–Y directions provides the optical image. In this configuration the tip is made of tapered glass. It is sharpened either by etching or by pulling. After coating it with aluminum, an opening is made at the apex by pressing it against a hard surface.

The most common application of this method is the registration of fluorescence induced by evanescent excitation. This kind of experimental setup is the most widely spread among researchers pursuing scanning near-field optical microscopy. There are advantages of such a "transparent fiber" approach: images are obtained with resolution much better than $\lambda/2$; the design is relatively simple; there is the possibility to obtain both shear force and optical images; the configuration is open for modification. The main disadvantage: resolution is rarely better than 50 nm for visible wavelenghts. Using an aperture size of less than 50 nm prohibitively decreases the amount of light that the fiber can emit. Moreover, even a small mechanical aperture will behave as a relatively large one because of the limited conductance of aluminum; the aperture edges are smeared. Lower sensitivity of infrared detectors in comparison with photon counting detectors presents a severe limitation for IR imaging with apertured probes, and would lead to a resolution limit of several hundred nanometers.

A second and somewhat complementary approach was described by Lahrech and co-workers.[6] They use a metallic (tungsten), vertically oscillating tip to modulate light scattering at the sample surface. The sample is illuminated by a focused IR beam incident at a high angle (80°). Such grazing illumination greatly reduces the intensity of the background light. Above the tip there is a reflection objective with a high numerical aperture. Signal at the IR detector is collected at the frequency of the tip oscillation. To control the tip-sample distance, an optical feedback loop is similar to the one described above is employed. Using this configuration Lahrech and coworkers where able to obtain 20 nm ($\lambda/600$!) resolution, which is greatly superior to that possible with the transparent fiber disign. Our own microscope is apertureless, like that of Lahreh and Wickramasinghe,[15] and is shown in Fig. 1.

Experimental

Our near-field microscope utilizes the scanning capabilities of a commercial atomic force microscope (Multimode AFM, Digital Instruments, Santa Barbara, CA). Figure 1 shows a schematic of the apparatus. The infrared light emitted by a carbon dioxide laser (wavelength appoximately 10 μm) is focussed by a parabolic mirror onto the end of a tungsten-coated cantilever probe perpendicular to the long axis of the probe. We use *p*-polarized light with a 73° angle of incidence. The spot size is approximately 100 μm and the radiation power is 20–100 mW. The probe is a commercial silicon probe (Silicon MDT, Moscow, Russia) coated with 25 nm of tungsten. This probe characteristics are length 130 μm, width 35 μm, resonance frequency 150 kHz, and radius of curvature of the tip 35 nm. These probe parameters are given as specified by the manufacturer. Driving the probe near its resonance frequency excited mechanical oscillation of the probe (100–200 nm total amplitude). Imaging of the surface of the sample in intermittent-contact (tapping) mode was performed simultaneously with

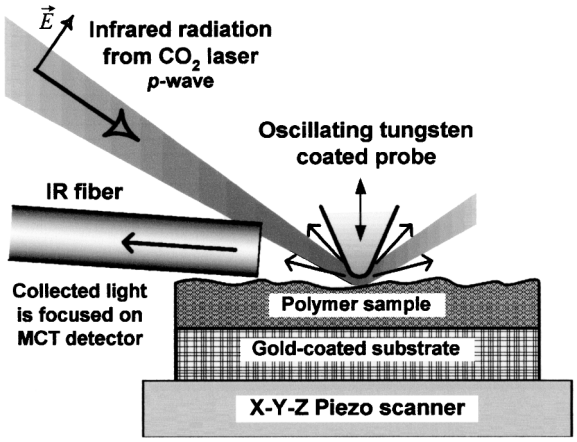

Fig. 1. The experimental apparatus. Light is brought in from the gas laser. A tip oscillates at frequency omega. Scattered light is collected through an IR fiber at an mercury cadmium telluride detector. A lock-in amplifier operating at the frequency of the oscillating tip collects the electrical signal from the detector. The presence of the tip modulates the scattering cross section of the surface immediately beneath the tip, which results in the detected signal.

the detection of the scattered infrared signal. An infrared-transparent multimode optical fiber (500 μm chalcogenide glass core) was placed near the probe (∼0.5 mm away) in order to collect light scattered at a small angle to the surface of the sample in the direction opposite to the incident beam (see Fig. 1). The fiber is slightly shifted sideways and tilted in the horizontal direction in order to allow propagation of the incident radiation. The positioning was restricted to a significant extent by the geometry of the commercial AFM used in our experiments. Light emitted from the optical fiber was focussed onto a MCT infrared detector (Graseby Infrared, Orlando, FL). The electrical signal from the detector was amplified by a lock-in amplifier (SR844, Stanford Research Systems, Sunnyvale, CA) at the frequency of the cantilever oscillation and collected by a computer simultaneously with AFM data. The use of an oscillating cantilever eliminated the dc background signal and provided the benefits of sensitive lock-in detection.

The polymer film sample was prepared by spin casting a 1.5 mg/mL solution of polystyrene–polydimethylsiloxane diblock polymer in CH_2Cl_2 at 3000 RPM using a Headway Research ED101 photo resist spinner. The molecular weight of the polymer was 144 kDa with 1:2.3 PDMP/PS mole ratio. A gold-coated microscope coverslip was used as the substrate in order to reflect infranred radiation and avoid excessive heating of the AFM.

Results and Discussion

The sample thickness was determined by making a scratch and imaging it using AFM; the sample was about 1 micron thick in the area of imaging. Topographic images of the sample reveal that ring-like structures have formed on the surface of the sample (Fig. 2). These rings have approximately 500 nm external diameter, 250 nm internal diameter and are 20 nm high. The formation of ring-like structures during solvent evaporation has been observed for many materials.[16] The cantilever oscillation phase signal collected simultaneously with the topography shows that the phase shift response is different

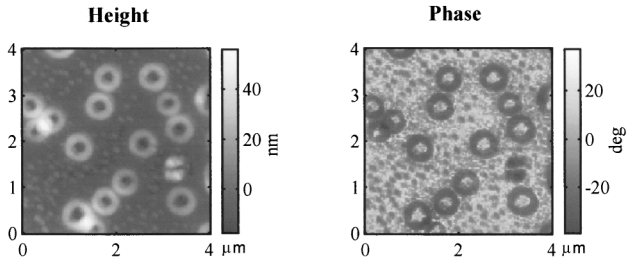

Fig. 2. AFM phase imaging of spun-cast polymer sample. (Poly (styrene-dimethylsiloxane) diblock polymer (PS-PDMS)) Phase contrast indicates that the high features have different mechanical properties than the flat area.

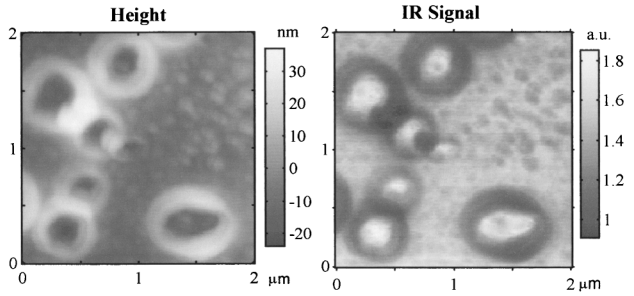

Fig. 3. Near-field signal collected at 935 cm^{-1}. Cantilever oscillation modulates the IR radiation scattered by the AFM probe. The amplitude of the detected modulation (IR signal) depends on the probe position. The IR signal is normalized to the intensity of the incident radiation. Data were collected using ∼50 mW of infrared radiation focused onto the cantilever by a parabolic mirror. The cantilever oscillation amplitude was 200 nm at 180 kHz. The ratio of the ac to dc signal on the MCT infrared detector was $\sim 5 \times 10^{-4}$. The detected ac component is $\sim 10^{-7}$ of the incident radiation power. High correlation between topography and scanning near-field signal, present on the maps here, is often thought to result from constant-gap scanning of topographic features.

on the rings than on the relatively flat surrounding area. The origin of the phase contrast could be due to different chemical composition of the rings compared with their surroundings, but it could also be caused by a larger compressibility of the rings that protrude from the sample.[17] A scattered infrared signal modulated by the oscillating probe (henceforth "infrared signal") was collected using the 935 cm^{-1} radiation of a CO_2 laser. At this frequency the PDMS component of the polymer has a noticeable absorption, in contrast to the PS block. Therefore the difference in scattered signal from the rings vs flat area might be taken to indicate variation in the chemical composition of the sample.[18,19] A map of the infrared signal collected simultaneously with the topographic map is shown in Fig. 3. These images were collected during intermittent-contact scanning of the surface with the cantilever oscillating at 180 kHz with 200 nm peak-to-peak amplitude. Topographical, protruding ring-like structures exhibit large variations in the associated infrared signals, with signal modulation of up to ca. 20% compared to flat area signals. The high correlation between the two images is thought to be result of constant-gap scanning

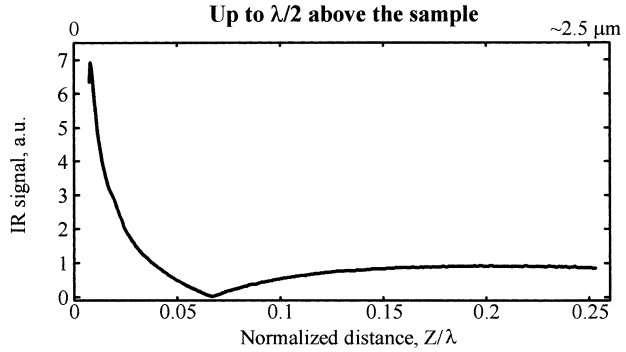

Fig. 4. At large distances above the sample the IR signal has non-exponential decay character. Infrared signal maps collected at different probe-sample distances exhibit a reversal of the contrast in the infrared signal. This supports the hypothesis that a significant component of contrast in the infrared image arises from the scanning probe following the topography.

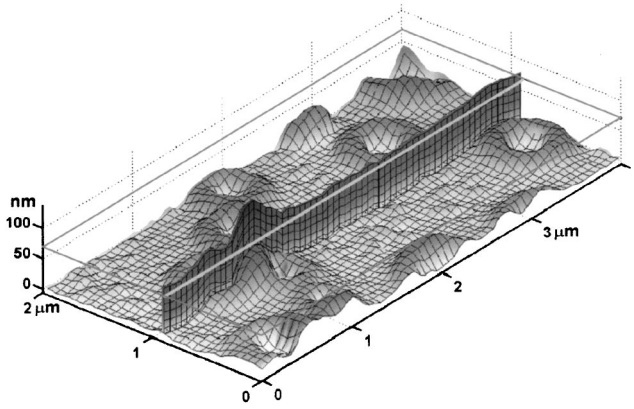

Fig. 5. The figure illustrates the interpolation procedure, which was used to obtain the infrared signal at a constant height. The two surfaces represent horizontal and vertical slices through a three-dimensional data matrix. Data were interpolated to a plane at a constant height. Gray line above the horizontal surface indicates the position of the plane.

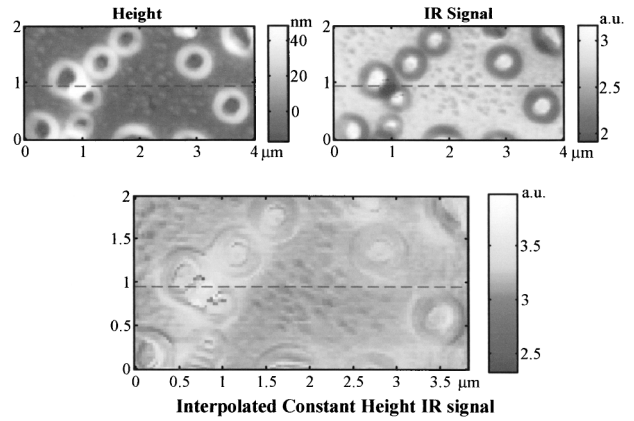

Fig. 6. Top left: surface topography. Top right: constant gap IR signal. Bottom: Constant height signal. The infrared signal image was created by elimination of topography-following coupling into near-field signal. The contrast from topographic structures is removed (the small differential signal from the ring edges is remaining probably due to a slight drift in the images used for interpolation.) In this bottom panel, the remaining small bumps between the rings are found to be PDMS-rich, indicating that the rings were composed of both blocks. The CO_2 laser is tuned to a frequency which is preferentially absorbed by the PDMS component. Cross section analysis shows the lateral spatial resolution to be about 100 nm.

of non-flat objects.[20,21] The signal dependence on the distance from the sample surface shows a fast decay close to the sample's surface (Fig. 4), which is followed by a non-monotonic (oscillatory) dependence. Additionally, we have collected the dependence of the infrared signal map on the mean separation between probe and the sample. During scanning, after each scan line, which probes the topography of the sample, we can lift the probe and repeat the probe trajectory at a desired height above the sample. Infrared signal images collected at two different heights (100 nm and 600 nm) show an obvious contrast reversal on these two images (data not shown) indicating that negative contrast on ring-like structures when the probe is close to the sample comes from the dependence of scattered light interference on the probe position, modulated by topography of the sample. Contrast reversal and non-monotonic distance dependence are also described by Weston[22] for aperture probe imaging in visible. In order to exclude topograhic contribution into our infrared signal one needs to perform scanning above the surface *without* following the topography.[23,24] Our instrument does not have such mode of imaging, therefore we used another approach.[25,26] We collected seven topographic and infrared signal maps at different probe-surface gap values, from 25 to 100 nm, that gives us three-dimensional signal dependence.[27] This range was large enough so we could interpolate our infrared signal to a plane above the surface. The procedure is illustrated on Fig. 5. The figure shows polymer surface with black lines indicating geometry of the surface and shades of gray corresponding to infrared signal. The vertical surface shows a slice through the three-dimensional matrix of data. The gray line indicates the position of the plane used for infrared signal interpolation. It is easy to see that the infrared signal correlates with topography of the sample and decays with increasing distance from the surface. The results of interpolation are presented on Fig. 6. For comparison, we show the sample's topography on the upper image and the interpolated infrared signal on the lower image. Almost all contrast found on the rings was eliminated, with some residual signal on the sides. A noticeable positive signal remains in the area where the rings intercept and a small negative signal is noticeable in the flat area between the rings in the middle of the image. When we perform an interpolation of our data, the protrusion on the surface is closer to the interpolating plane than the rest of the surface, as can be seen on Fig. 5. Therefore, the positive signal on Fig. 6 could be a result of such proximity (FDTD calculations support this hypothesis). Small, negative contrast features are discernable in the flatter center of the image, where there should be no contrast modulating mechanism as found for the large protruding feature in the interpolated infra-

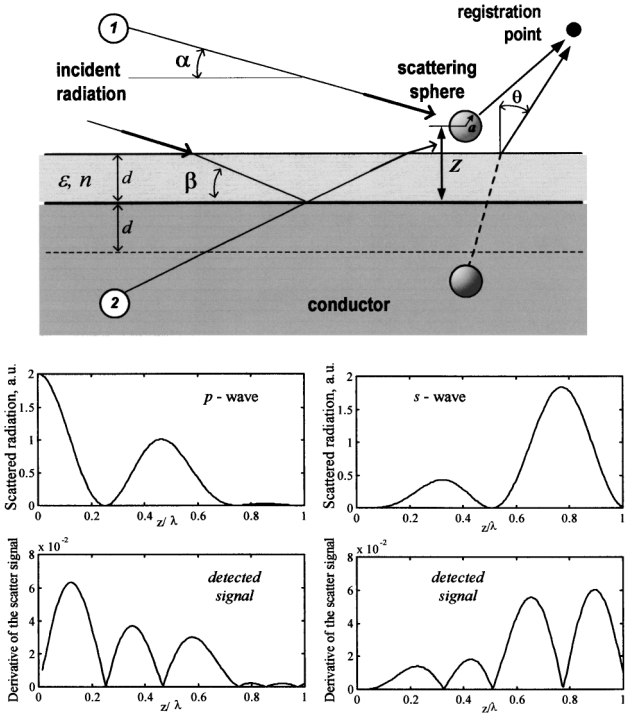

Fig. 7. Top Panel. Light scattering by a conductive sphere near a conductive surface covered by an absorptive layer. Mirror images of the incident radiation, dipole induced in the conductive sphere and dipole induced in the layer which coats the perfect conductor interface are used to calculate scattered radiation. Bottom panel. Four plots showing calculated scattering, without the absorbing layer. In these calculataions, $\alpha = 15°$, $\alpha = \lambda/100$, $\lambda = 10$ μm. Periodic signal corresponds qualitatively to that seen in Fig. 4.

red signal.[28] This suggests that negative contrast observed on small features might arise due to local variations of optical properties. The observed variations allow us to conclude that spatial resolution is approximately $\lambda/100$. We note that this value is larger than the distance from the surface to the plane where the signal was interpolated (~70 nm).

Theoretical Models. In order to predict how the scattered signal depends on imaging conditions we first devise a simple analytical model consisting of a plane electromagnetic wave incident on a scattering probe and an infinitely wide absorptive layer placed on semi-infinite conductor. Scattering from the probe is calculated using a model for scattering by a small conductive sphere. Scattering from such probe consists of fields emitted by magnetic and electric dipoles, placed at the middle of the sphere.[29] The boundary conditions for the electric vector at the surface of the perfect conductor allow us to further simplify the model by replacing the perfect conductor with a mirror image of the absorptive layer, scattering probe and incident wave (see Fig. 7). The electric vector at the registration point is calculated as a sum of the electric vectors due to scattering of the original plane weve, the attenuated and phase shifted wave propagating through the layer of the sample, and mirror images of those plane waves by two probes, as illustrated on Fig. 7. Spherical components (r, θ, ϕ) of the electric vector of scattered radiation were calculated using Eg. 1.

$$\vec{E}_{\mathrm{sc}}(r,\theta,\phi) = \frac{k^2 a^3 e^{ikr}}{r} \begin{pmatrix} 0 \\ E_x^{\mathrm{inc}}\cos\phi(\cos\theta - \sin\alpha/2) \\ \quad + E_y^{\mathrm{inc}}\sin\phi(\cos\theta - \sin\alpha/2) \\ \quad - E_z^{\mathrm{inc}}(\sin\theta + \cos\alpha\cos\phi/2) \\ E_x^{\mathrm{inc}}\sin\phi(-1 + \cos\theta\sin\alpha/2) \\ \quad + E_y^{\mathrm{inc}}(\cos\phi(1 - \cos\theta\sin\alpha/2) \\ \qquad + \sin\theta\cos\alpha/2) \\ \quad + E_z^{\mathrm{inc}}\cos\theta\sin\phi\cos\alpha/2 \end{pmatrix} \quad (1)$$

where E^{inc} are Cartesian components of the electric vector of the incident plane wave, k is the magnitude of the wavevector, a is the radius of the sphere, α is the angle between the wavevector and the surface, and r is the distance between the observation point and the origin. When the conductive sphere is shifted from the origin, the scattered field is calculated by transforming the coordinate system. We averaged intensity $|E_{\mathrm{sc}}|^2$ over a range of angles θ and ϕ in order to simulate the light collected in the experiment. Calculations were performed as a function of probe separation from the surface. Since in the experiment we collected the ac component while dithering probe in direction perpendicular to the surface, the calculated signal was differentiated with respect to the separation variable. Graphs at the bottom of Fig. 7 show the calculated intensity and z-derivative of this intensity for p-and s-polarized incident radiation in the absence of the absorbing layer. Graphs are labeled to indicate the polarization of the incident plane wave. These calculations demonstrate that s-polarized light produces no signal when the probe is close to the surface, thus it is not suitable for near-field signal detection. Calculations performed with absorbing layer atop the perfect conductor provide the distance and absorption dependence of the scattered signal and indicate that interference of the light scattered from the probe and its reflection is a possible cause of topography-related artifacts.

In order to calculate the scattering signal for samples with topographic features on the surface we use the finite difference time domain method (FDTD). In our implementation FDTD solves the Maxwell curl equations (Eq. 2) for isotropic non-magnetic media on a three-dimensional grid by propagating electromagnetic fields through the calculation space. We use the FDTD algorithm according to Taflov.[30]

$$\begin{aligned} \frac{\partial \vec{H}}{\partial t} &= -\frac{1}{\mu_0}\left(\nabla \times \vec{E}\right) \\ \frac{\partial \vec{D}}{\partial t} &= \frac{1}{\varepsilon}\left[\left(\nabla \times \vec{H}\right) - \sigma \vec{E}\right] \end{aligned} \quad (2)$$

In FDTD the Cartesian components of electric and magnetic fields (we calculate the E and H fields) are interlaced in space and time in such way that finite differences are calculated as center-difference, and the solution to the Maxwell equations is accurate to second order.[30] Electric field components are calculated on faces of the calculation grid while magnetic field components are calculated on edges, as illustrated on Panel A

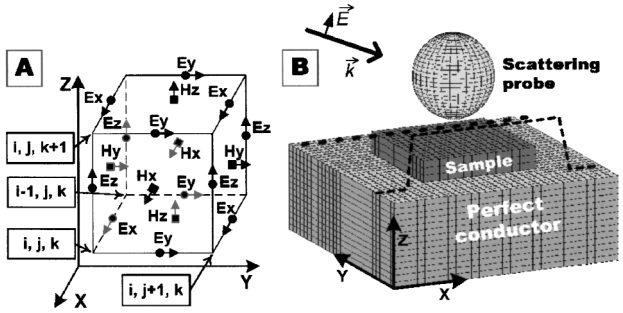

Fig. 8. Panel A shows the arrangement of the electric and magnetic field components, utilized in FDTD calculations (so-called Yee cell[30]). Panel B demonstrates the geometry used in FDTD calculations. The scattering probe scans at the interface. Dashed lines indicate possible scanning directions: at a constant height above the conductor or at a constant probe-surface gap.

of Fig. 8. Also, the magnetic field is displaced in time by 1/2 of a time step compared to the electric field. The resulting finite-difference equations for updating x-component of the fields at the next time step for dielectric or conductive materials are:

$$H_x^{n+1/2}(i,j,k) = H_x^{n-1/2}(i,j,k) + \frac{dt}{\mu_0}\left[\left\{E_y^n(i,j,k+1/2) - E_y^n(i,j,k-1/2)\right\}/dz - \left\{E_z^n(i,j+1/2,k) - E_z^n(i,j-1/2,k)\right\}/dy\right] \quad (3a)$$

$$E_x^{n+1}(i,j,k) = \left[1-\frac{\sigma(i,j,k)dt}{\varepsilon(i,j,k)}\right]E_x^n(i,j,k) + \frac{dt}{\varepsilon(i,j,k)} \times\left[\left\{H_z^{n+1/2}(i,j+1/2,k) - H_z^{n+1/2}(i,j-1/2,k)\right\}/dy - \left\{H_y^{n+1/2}(i,j,k+1/2) - H_y^{n+1/2}(i,j,k-1/2)\right\}/dz\right] \quad (3b)$$

where dt is the time step, dx, dy, dz are the grid sizes, $\varepsilon(i, j, k)$ and $\sigma(i, j, k)$ are local values of the permittivity and conductivity. In the equations above, i, j, and k indexes for electric field update equation correspond to $\{(i + 1/2) \cdot dx, j \cdot dy, k \cdot dz\}$ positions in space, and $\{i \cdot dx, (j + 1/2) \cdot dy, (k + 1/2) \cdot dz\}$positions for the magnetic field update equation. The superscripts of the field variables indicate the time step, for example, $(n + 1/2)$ superscript corresponds to $(n + 1/2) \cdot dt$ point in time. Similar update equations can be written for other Cartesian components of the EM field.[30] The calculation space consists of three regions: the total field region, the scattered field region and an absorbing boundary region, see Fig. 9, top panel. Conductive, dielectric or dispersive objects are placed in the total field region, where the plane EM wave interacts with objects, creating scattered waves. The scattered field region, which surrounds the total field region, is used to model the incident plane wave and to separate the scattered waves. The incident radiation is calculated analytically, which allows us to place the interface of dielectric or conductive half-space in the calculation space. In order to avoid scattered field reflection at the boundary of computational space, a perfectly matching layer is used for an absorbing boundary.[31] A plane wave with the desired polarization and direction of propagation is switched on at time '0' at the boundary of computational space. Electric and magnetic fields are calculated with a time step given by

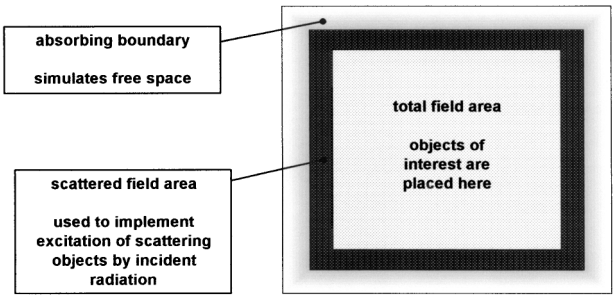

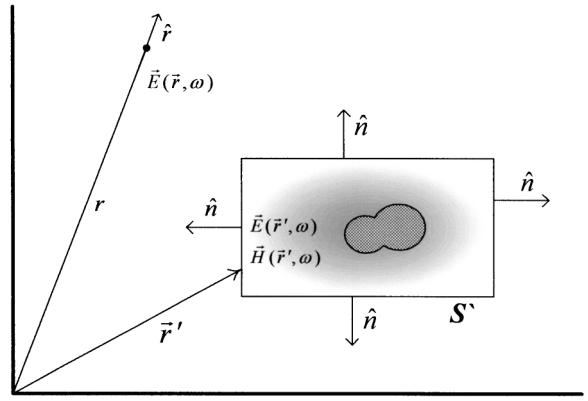

Fig. 9. Top: The calculations volume is separated into three regions. Bottom: Near-field to far-field transformation in the frequency domain.

numerical stability condition, until the fields are harmonic[32] in the calculation space. Numerical stability is achieved for time steps satisfying[30]

$$\Delta t \le \left(c\sqrt{\Delta x^{-2} + \Delta y^{-2} + \Delta z^{-2}}\right)^{-1} \quad (4)$$

where c is a speed of light, Δx, Δy and Δz are grid sizes. Scattered fields in the far field are calculated by using frequency domain near-field to far-field transformation:[33]

$$\vec{E}(\vec{r},\omega) = \frac{j\omega\mu_0}{4\pi r}\iint_S\left\{\begin{array}{l}\hat{r}\times\hat{r}\times\left[\hat{n}\times\vec{H}(\vec{r}',\omega)\right] \\ -\frac{1}{\eta_0}\hat{r}\times\left[\hat{n}\times\vec{E}(\vec{r}',\omega)\right]\end{array}\right\}\exp\left[-\frac{j\omega(r-\hat{r}\cdot\vec{r}')}{c}\right]dS' \quad (5)$$

where $\vec{r}$ is a vector to the observation point, ω is a radial frequency of the EM radiation, S is a surface surrounding the scattering objects, r is a distance to the observation point, μ_0 is the permeability of vacuum, η_0 is the impedance of vacuum, $\vec{r}'$ is a vector to a point on the surface S, $\hat{r}$ is a unit vector in the direction of $\vec{r}$ and $\hat{n}$ is an outward normal vector to the surface S. See Fig. 9, bottom panel. In order to use transformation (5) we calculate the frequency domain components of the EM radiation. First, we interpolate the field values in space and time to the surface placed inside the scattered field region. The interpolated time-dependent scattered field components are used to calculate frequency–domain amplitudes at a frequency equal to the frequency of the incident plane wave using

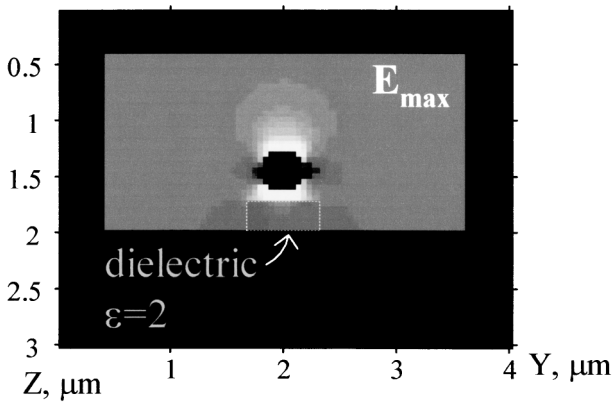

Fig. 10. ANSIM probe tip under illumination, showing feild enhancement for conductive tip above square dielectric object. Figure shows a 2D cross section through the 3D calculation space. Dark sides of the image correspond to the scattering field area and the perfect conductor, located below the dielectric. The height of the tip above the surface is 100 nm.

a discrete Fourier transform. The resulting field distribution on the chosen surface are used in the transformation, given above. Since this transformation propagates fields in a vacuum, to account for the presence of a conductive interface we reflect the fields propagated into the region occupied by half-space conductor. The scattered signal measured in the experiment is computed by integrating the intensity of the calculated scattered signal in the direction of detection.

In FDTD calculations, dielectric and absorptive objects are placed on the surface of perfect conductor, and conductive scattering probe is placed nearby and scanned across the surface. At each lateral position of the probe we calculate the scattered signal at different probe–sample separations in order to obtain the ac component of the scattering signal. Probe scanning can be performed by two modes: constant height above the perfect conductor interface or constant probe-sample gap. Panel B of Fig. 8 shows the geometry of the three-dimensional model used in our FDTD calculations.

Employing this theory, it is easy to observe that the dielectric objects act as antennas to enhance the field strength in their vicinity, see Fig. 10. This figure show distribution of the maximum electric field calculated during the plane wave propagation across the sample. Figure 11a shows the geometry of the three-dimensional model used in the FDTD calculation illustrated in Fig. 11b. It is apparent that scanning a tip at a constant height across dielectric and absorptive objects can be used for imaging, and that the response can be modeled, including field attenuation. Figure 12 illustrates the detection of dielectric contrast in 2D scanning at constant height above a *flat* but heterogeneous surface. The top panel shows the scattering geometry, while the bottom panel shows the scattered intensity taken along Y axis. The magnitude of the signal does not scale with the dielectric constant. Intensity distribution is nearly identical along X (not shown).

Conclusions. A spin cast sample of poly (dimethylsiloxane-styrene) diblock polymer was characterized by atomic force microscopy and apertureless near-field infraed microscopy. Characteristic topograhic features (rings) exhibit both AFM phase contrast and infrared contrast. The scattered IR radiation intensity changes in a non-monotonic fashion upon probe withdrawal from the surface. The lateral contrast of the IR signal is correlated with the topography for images collected with constant tip-sample gap. Data interpolation to the constant height scanning removes most of the IR contrast.

We employed a model including a small conductive sphere scattering near a dielectric layer on top of a semi-infinite perfect conductor to simulate the effect of the layer thickness and interference effects on the scattered infrared signal. Imaging at constant tip-sample gap for non-flat samples will result in a topography-correlated near-field signal.

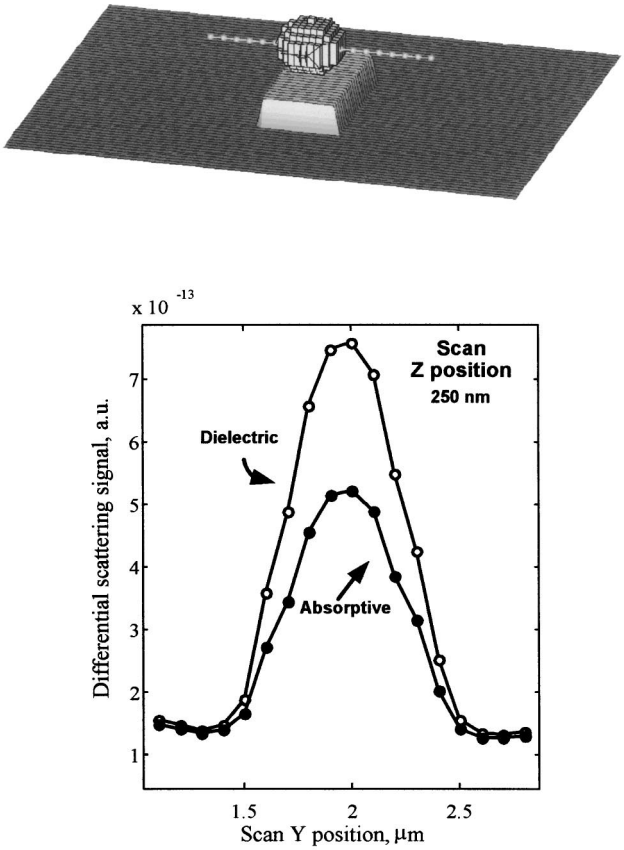

Fig. 11. Top: In the simulation the tip scans at constant height above the sample resting on the conductive surface, as illustrated by the dotted line extending from the sphere (tip) above a box (sample) on top of the substrate (dark plane). Bottom: Derivative of scattering signal calculated at constant height above the surface for dielectric and absorptive object. The infrared signal attenuation for an absorptive object is larger than for a bare layer of the same thickness. The radiation wavelength is 10 μm, the sphere radius is 250 nm. The absorption coefficient of the absorptive object is 300 m OD/micron, which in the simulation serves to illustrate the basic observation but exceeds the actual coefficient for the polymeric sample in this study. The real part of permitivity for the Lorenztian was same as for the dielectric. Scanning at a higher height would give a similar, albeit smaller signal, but the edge resolution would be worse.

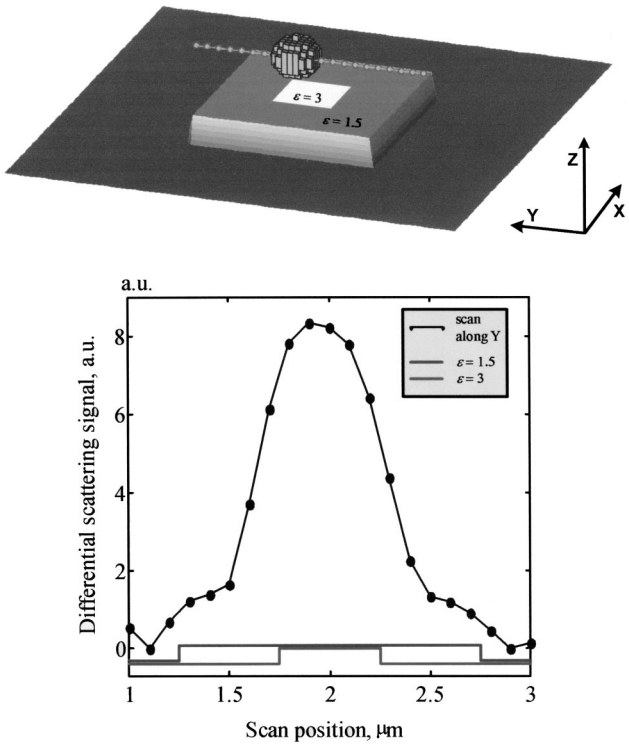

Fig. 12. Dielectric contrast in 2D scanning at constant height. Top: Scattering geometery. Bottom: Scattered intensity taken along Y axis. Magnitude of the signal does not scale with the dielectric constant. Intensity distribution is nearly identical along X (not shown).

The finite-difference time-domain method was used to model the scattered infrared radiation for samples with topographic features. Constant height scanning results in signal which depends on absorption of the object on the surface. Constant gap scanning gives a topography correlated signal.

We gratefully acknowledge the NSF (CHE-9816820 and PHYS-0103048), the Office of Naval Research (ONR N001-96-1-0735), and the Office of Army Research (DAAD16-99-C-1036) for financial support. BA acknowledges a Mellon predoctoral fellowship. We are grateful to Steven Pollack for providing the polymer sample.

References

1 T. Cosgrove, *J. Chem. Soc., Faraday Trans.*, **86**, 1323 (1990)

2 A. W. Adamson, "Physical Chemistry of Surfaces," John Wiley & Sons (1982).

3 D. W. Pohl, W. Denk, and M. Lanz, *Appl. Phys. Lett.*, **44**, 651 (1984).

4 U. Durig, D. W. Pohl, and N. Rohrer, *J. Appl. Phys.*, **59**, 3318 (1986).

5 E. Betzig, A. Lewis, A. Harootunian, M. Isaacson, and E. Kratschmer, *Biophys. J.*, **49**, 269 (1986).

6 A. Lahrech, R. Bachelot, P. Gleyzas, and A. C. Boccara, *Opt. Lett.*, **21**, 1315 (1996).

7 D. A. Christensen, *Uitramicroscopy*, **57**, 189 (1995); A.V. Zvyagin, M. Ohtsu, *Opt. Commun.*, **133**, 328 (1997).

8 R. X. Bian, R. C. Dunn, and X. S. Xie, *Phys. Rev. Lett.*, **75**, 4772 (1995).

9 D. Courjon and C. Bainier, *Rep. Prog. Phys.*, **57**, 989 (1994).

10 R. J. Hamers, *J. Phys. Chem.*, **100**, 13103 (1996).

11 E. Wolf and M. Nieto-Vesperinas, *J. Opt. Soc. Am.*, **2**, 886 (1985).

12 E. H. Synge, *Phil. Mag.*, **6**, 356 (1928).

13 H. A. Bethe, *Phys. Rev.*, **66**, 163 (1944).

14 E. A. Ash, and G. Nichols, *Nature.*, **237**, 510 (1972).

15 F. Zenhausern, M. P. O'Boyle, and H. K. Wickramasinghe, *Appl. Phys. Lett.*, **65**, 1623 (1994).

16 J. Hahm, and S. J. Sibener, *Langmuir*, **16**, 4766 (2000).

17 S. N. Magonov, and D. H. Reneker, *Annu. Rev. Mater. Sci.*, **27**, 175 (1997).

18 B. Dragnea, J. Preusser, W. Schade, S. R. Leone, W. D. Hinsberg, *J. App. Phys.*, **86**, 2795 (1999).

19 B. Knoll and F. Keilmann, *Nature*, **399**, 134 (1999).

20 B. Hecht, H. Bielefeldt, Y. Inouye, D. W. Pohl, and L. Novotny, *J. Appl. Phys.*, **81**, 2492 (1997).

21 B. Knoll, F. Keilmann, A. Kramer, R. Guckenberger, *Appl. Phys. Lett.*, **70**, 2667 (1997).

22 K. D. Weston, and S. K. Buratto, *J. Phys. Chem. B*, **101**, 5684 (1997).

23 B. Hecht, H. Bielefeldt, Y. Inouye, D. W. Pohl, and L. Novotny, *J. Appl. Phys.*, **81**, 2492 (1997).

24 L. Novotny, B. Hecht, and D. W. Pohl, *Ultramicroscopy*, **71**, 341 (1998).

25 B. B. Akhremitchev, S. Pollack, and G. C. Walker, *Langmuir*, **17**, 2774 (2001).

26 H. Hatano, Y. Inouye, and S. Kawata, *Opt. Lett.*, **22**, 1532 (1997); C. E. Jordan, S. J. Stranick, L. J. Richter, and R. R. Cavanagh, *J. Appl. Phys.*, **86**, 2785 (1999).

27 J. Levy, A. Cohen, and D. D. Awschalom, *Rev. Sci. Instrum.*, **66**, 3385 (1995).

28 H. Furukawa and S. Kawata, *Op. Commun.*, **132**, 170 (1996).

29 J. D. Jackson, "Classical Electrodynamics," John Wiley & Sons, Inc., New York (1975), pp. 411-418.

30 A. Taflove, "Computational Electrodynamics: the Finite-difference Time-domain Method," Artech House, Boston (1995).

31 J.-P. Berenger, *J. Comp. Phys.*, **127**, 363 (1996).

32 In order to satisfy this criterion, we integrate electric field components in time over one period for every location. For harmonic fields, this should give zero, and in actual calculations, the results of such averaging were compared to the amplitude of the incident radiation to obtain an "unharmonicity" error. Calculations were performed until such calculated error was less then the specified threshold value, usually 1% of the incident amplitude. We note that the number of calculated time steps according to this criterion was approximately the same as for a more commonly used criterion, which states that number of time steps should be greater of equal 10 *N*, where *N* is the maximum number of grids along the coordinate axes.

33 L. G. Maloney and G. S. Smith, in "Advances in Computational Electrodynamics:, the Finite-difference Time-domain Method," ed by Taflove, Artech House, Boston (1998).